

Cite this: *RSC Adv.*, 2015, 5, 9143

Superior ethanol-sensing behavior based on SnO₂ mesocrystals incorporating orthorhombic and tetragonal phases

C. D. Gu,^{*ab} H. Zheng,^a X. L. Wang^{ab} and J. P. Tu^{ab}

SnO₂ mesocrystals with mixed phases (*i.e.*, tetragonal and orthorhombic phases) and nanoporous structures have been successfully synthesized *via* a facile annealing topotactic transformation from SnO precursors under ambient-pressure and a moderate temperature range of 400–600 °C. The morphology of the mesocrystal precursor possesses a hydrangea ball or multilayer pancake structure, which is determined by a novel ionothermal strategy using choline chloride/urea based deep eutectic solvent (DES) as the reaction medium and water as the morphology controlling agent. The self-assembly of SnO mesocrystals is based on a "non-classical crystallization" process involving an oriented attachment mechanism. The polarity dependent self-assembly of SnO mesocrystals in the reaction system is also highlighted. Significantly, the mixed phase and nanoporous SnO₂ mesocrystal exhibits superior ethanol sensitivity compared with that of the SnO₂ with a single tetragonal phase or a solid structure. The sensitivity of the SnO₂ sample obtained at 400 °C is as high as 28.06 under 100 ppm ethanol and an optimum operation temperature of 300 °C, standing out from most of the state-of-the-art SnO₂ nanomaterials, which is due to the incorporation of orthorhombic and tetragonal phases and the porous structure. Furthermore, the SnO₂ mesocrystal with the mixed phases is also demonstrated to be a good selective ethanol sensor to effectively discriminate ethanol from acetone, methanol, and benzene.

Received 6th November 2014
Accepted 22nd December 2014

DOI: 10.1039/c4ra13940b

www.rsc.org/advances

1. Introduction

Chemiresistive gas sensors based on metal oxides have been widely investigated for decades driven by their practical applications in monitoring volatile organic compound vapors, such as acetone, alcohol, and so on, because they can offer good sensing properties and can be easily mass-produced.^{1–8} Among the different semiconducting metal oxides, SnO₂ is one of the most important and extensively used for gas sensors due to its low operating temperatures, high sensitivities, quick gas response, and low costs.^{1,7–10} In general, there are two gas-detection mechanisms using gas sensors. One utilizing changes in sensor material by the interaction with gases, which is based on the reversible oxidation–reduction reaction of the gas with the surface of the oxide surface to cause a significant resistance change in proportion to the gas concentration.^{2,11} The other utilizing signals are obtained from the gas itself, *i.e.* the cataluminescence-based gas sensors.^{12–17} According to the chemiresistive gas-detection mechanism of metal oxides,

specific surface area, porosity, grain size, structure, and morphology are the key parameters that are generally manipulated to optimize the sensing performance of the SnO₂-based gas sensor.^{18–23} SnO₂ is known as having three polymorphs: tetragonal SnO₂ (t-SnO₂), orthorhombic SnO₂ (o-SnO₂), and cubic SnO₂.²⁴ Under normal conditions, SnO₂ exists in the most important form of a rutile tetragonal crystal phase known as cassiterite. The t-SnO₂ has been extensively studied in terms of its optical, electrical, and gas-sensing properties. However, the effect of polymorphs on the gas sensing performance of SnO₂ is seldom reported compared with the other parameters as shown above.^{25–27}

The t-SnO₂ under ambient conditions is stable while it is difficult to obtain o-SnO₂ through traditional methods under low pressure and temperature.^{26,28} The formation of the orthorhombic phase SnO₂ depends on a number of important synthetic parameters, such as high pressures and temperatures. Using a pressure cell equipped with a heating stage, Suito *et al.*²⁹ observed a transformation to an orthorhombic phase at a pressure of 15.8 GPa and a temperature of 800 °C. Although the orthorhombic phase was originally observed in high-pressure experiments, it has been recently produced in thin-film and nanoparticle samples.³⁰ The nucleation of the orthorhombic phase is not driven by the particle size because even when the particle size of the cassiterite SnO₂ was reduced to as low as 2.5 nm, the orthorhombic phase was still not observed.³¹ The

^aState Key Laboratory of Silicon Materials, Key Laboratory of Advanced Materials and Applications for Batteries of Zhejiang Province, School of Materials Science and Engineering, Zhejiang University, Hangzhou 310027, China. E-mail: cdgu@zju.edu.cn; Fax: +86 571 87952573; Tel: +86 571 87952573

^bCyrus Tang Center for Sensor Materials and Applications, Zhejiang University, Hangzhou 310027, China

mixed phase (*i.e.*, tetragonal and orthorhombic phases) coexistence SnO_2 has been synthesized,^{32,33} and the formation of orthorhombic phase was attributed to the extrinsic strains in thin film experiments.^{34,35} However, in the unconstrained Fe-doped SnO_2 nanoparticles, Zhang *et al.*³⁶ found the electron beam irradiation can induce a tetragonal-orthorhombic phase transition, which is due to the locally increased temperature and pressure formed in the particle aggregation. Significantly, in terms of gas sensor performance, Sangaletti *et al.*^{25,37} and Hu *et al.*²⁷ reported that SnO_2 in mixed phases with the coexistence of t- and o-phase structures exhibits better sensitivity for specific gases than does the tetragonal rutile-type structure.^{25,38} On the contrary, Ahn *et al.*²⁶ reported that the mixed phase SnO_2 powder has detrimental effect on the sensitivity towards hydrogen gas, which was attributed to an increased number of planar defects in the microstructure and a change in species of the oxygen absorbents on the surface layer of the SnO_2 . Therefore, the gas sensing property of the orthorhombic phase SnO_2 is still not completely researched, and a more detailed analysis is needed to explore the correlation between the crystallographic structure and the gas sensing performance.³⁸

Some authors have demonstrated that tin monoxide can be a precursor in the ambient-pressure synthesis of the orthorhombic phase of SnO_2 .³⁰ Krasevec *et al.* discovered the orthorhombic phase SnO_2 in annealed SnO thin film.³⁴ Lamelas showed that the metastable o- SnO_2 was produced by the oxidation of the mechanically milled litharge-phase SnO .³⁰ Lamelas *et al.*^{30,32} hold the view that tin monoxide was the critical precursor in the formation of the orthorhombic phase at ambient pressure. However, directly annealing SnO particles at ambient-pressure to produce the metastable o- SnO_2 has not been realized.

Our recent study showed that hydrangea-like micro-sized SnO particles can be synthesized *via* a facile ionothermal strategy in a choline chloride/urea (CU) formed deep eutectic solvent (DES).³⁹ DES represents an attractive alternative to room temperature ionic liquids, sharing most of their remarkable advantages, such as low cost, facile synthesis, nontoxicity, and biodegradation.^{40–42} DESs have been known as designer solvents to create well-defined nanomaterials including shape-controlled nanoparticles and electrodeposited films.^{40,41,43–48} In this study, the self-assembly (SA) process of SnO mesocrystals is controlled *via* an ionothermal method in the CU system. The SnO_2 mesocrystals incorporated with o- and t-phases have been successfully prepared for the first time by directly annealing the SnO precursors at ambient-pressure condition. In addition, the superior ethanol sensitivity of the mixed phase SnO_2 mesocrystals is also demonstrated.

2. Experimental

2.1 Preparation of samples

The ionothermal synthesis process for the SnO particles can be found in our previous study.³⁹ In this study, further innovation for the ionothermal strategy was proposed by using water as the SnO morphology controlling agent. A typical procedure is shown as follows. The starting materials are choline chloride

(ChCl), urea and $\text{SnCl}_2 \cdot 2\text{H}_2\text{O}$, which were used as received without further purification. The ChCl/urea based DES (CU) was obtained by mixing the ChCl and urea (A.R., Aladdin) stoichiometrically in a molar ratio of 1 : 2 in the condition of stirring at 80 °C to form a homogeneous colorless liquid. Then, 2.25 g $\text{SnCl}_2 \cdot 2\text{H}_2\text{O}$ was dispersed in 100 ml CU with magnetic stirring to form a homogeneous white emulsion, which contains about 1% water revealed by Karl-Fischer titration (Zhibo Zhenggong titrators WS-3). Another two parallel experiments were carried out with water content of ~5 and ~15%, respectively. Then, the mixture was heated to 100 °C with a heating rate of 5 °C min^{−1} under vigorous stirring. After the mixture was maintained at 100 °C for 60 min, the color of the mixtures changed from cream white to brown. The brown precipitates were washed alternately with water and methanol, centrifuged and dried. For convenience, the products obtained in different water contents will be hereafter denoted as 1-SnO, 5-SnO, and 15-SnO, respectively, where the prefix number indicates the water content. SnO_2 samples were prepared by annealing the SnO powders in a traditional muffle furnace. The furnace was slowly heated to 400, 600, and 900 °C at a rate of 10 °C min^{−1} and kept for 2 h, respectively. Here, we use x-y-SnO₂ to represent the specific sample, where x represents the water content and y represents the temperature at which the sample was annealed. After the furnace was cooled to room temperature, the reaction products were collected.

2.2 Microstructure characterization

The as-synthesized powders were characterized by X-ray diffraction (XRD, Rigaku D/max-2550 with Cu-K α radiation), field emission scanning electron microscopy (FE-SEM, Hitachi S-4800), and high-resolution transmission electron microscopy (HR-TEM, Tecnai F20), respectively. The specific surface area of the porous SnO_2 samples was estimated using the Brunauer–Emmett–Teller (BET) equation based on the nitrogen adsorption isotherm obtained with a Belsorp-max (AUTOSORB-IQ-MP). The classical pore size model developed by Barrett, Joyner and Halenda (BJH) was used to evaluate the pore size distribution of the SnO_2 samples.

2.3 Gas sensing properties tests

The gas sensor was fabricated as follows. A proper amount of the annealed SnO_2 particles were ground with several drops of deionized water in an agate mortar to form a paste. The sensors were made by a coating ceramic tube with paste to form a thin sensing film. The ceramic tube was installed with a pair of gold electrodes and four Pt wires on each end of the tube. A Ni–Cr alloy filament was put through the tube and used as a heater by tuning the heating voltage. Gas sensing tests were performed on a static test system (WS-30A, WeiSheng Electronics Co. Ltd., ZhengZhou, China) using air as the reference and diluting gas at a relative humidity (RH) of 32%. The sensor response is defined as the ratio $S = R_a/R_g$, where R_a and R_g are the electrical resistances of the sensors in air and in gas, respectively. The time taken by the sensor resistance to change from R_a to $R_a - 90\% \times (R_a - R_g)$ was defined as response time (t_{res}) when the

ethanol gas was introduced to the sensor. The time taken by the sensor resistance to change from R_g to $R_g + 90\% \times (R_a - R_g)$ was defined as recovery time (t_{rec}) when the ambience was replaced by air.

3. Result and discussion

Fig. 1 shows the XRD patterns of the as-prepared SnO samples under different water contents (a) and the SnO samples under different annealing conditions (b–e). The reference patterns of the orthorhombic SnO₂ (JCPDS #29-1484), the tetragonal SnO₂ (JCPDS #41-1445), and the tetragonal SnO (JCPDS #06-0395) are also given for comparison. As shown in Fig. 1a, all diffraction peaks of the ionothermal products are perfectly assigned to the tetragonal SnO phase (JCPDS #06-0395, $a = b = 0.3802$ nm, $c = 0.4836$ nm). It should be noted that the prepared SnO is stable at room temperature. The sample held the same XRD patterns as the as-prepared state when kept about one month in air. The dependence of the intensity ratios of (101)/(110) peaks ($I_{(101)}/I_{(110)}$) on the water content in the preparation is indicated in Fig. 1a. It is clearly evident that with increasing water content, the ratio of $I_{(101)}/I_{(110)}$ decreases from 1.67 (1-SnO), 1.12 (5-SnO), to 1.07 (15-SnO). The ratio of $I_{(101)}/I_{(110)}$ peaks in a standard powder diffraction pattern of t-SnO powder is about 2.86, which represents the value for the isotropic polycrystalline SnO. It indicates that the SnO grows anisotropically when more water exits in the reaction system, and the (110) planes are preferentially oriented parallel to the surface of the XRD supporting substrate. At moderate annealing temperatures (400 and 600 °C) for about 2 h, both t- and o-phases of SnO₂ appeared simultaneously, as shown in Fig. 1b–d. Hu *et al.*²⁷ recently obtained the mixed phase SnO₂ nanorods assembled with SnO₂ nanocrystals by annealing the SnC₂O₄ slurry-like precursor. The two SnO₂ polymorphs are the rutile-type SnO₂ (JCPDS 41-1445) with lattice parameters $a = 0.4738$ nm and $c = 0.3187$ nm and the orthorhombic SnO₂ (JCPDS 29-1484) with lattice parameters $a = 0.4714$ nm, $b = 0.5727$ nm, and $c = 0.5214$ nm. The content of o-SnO₂ in the mixed phase 15-400-SnO₂ and 15-600-SnO₂ is measured to be about 38.7 wt% and 29.0 wt%, respectively, which is revealed by the Rietveld analysis of XRD powder patterns. For the sample of 1-400-SnO₂, the weight fraction of o-SnO₂ in the sample of 1-400-SnO₂ is about 40.4 wt%. The correlation between the content of o-SnO₂ and the gas sensor performance will be highlighted in this study. At a higher temperature of 900 °C, o-phases of SnO₂ disappeared and uniquely t-phases of SnO₂ are formed (Fig. 1e). Shek *et al.*⁴⁹ found the appearance of the orthorhombic SnO₂ phase during the transformation of disordered SnO₂ to tetragonal SnO₂ (rutile) under post-annealing at 300–600 °C in air. It is also suggested that less atomic rearrangements in the transformation of tetragonal SnO to tetragonal SnO₂ may be necessary for the formation of orthorhombic lattice than for the formation of cassiterite.³⁸ In our case, o-phases of SnO₂ also can be seen as an intermediate phase during the transformation of tetragonal SnO to tetragonal SnO₂, which is the high temperature stable phase.

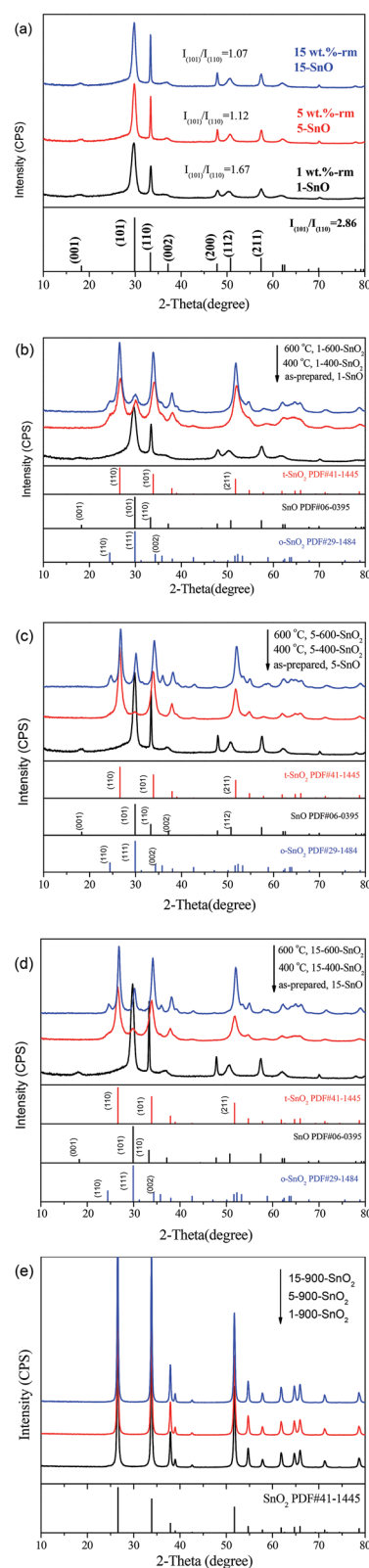


Fig. 1 XRD patterns of the as-prepared SnO samples (a) and the SnO samples under different annealing conditions (b–d). (e) is the XRD patterns of the as-prepared SnO samples after annealing at 900 °C. The reference patterns of the orthorhombic SnO₂ (JCPDS #29-1484), the tetragonal SnO₂ (JCPDS #41-1445), and the tetragonal SnO (JCPDS #06-0395) are also given for comparison.

Fig. 2 gives the SEM images of as-prepared SnO samples from different reaction systems with various water contents (a, d and g) and their corresponding annealing products. The morphology of the as-prepared SnO is highly depended on the water content in the reaction system. For the CU system without adding extra water, *i.e.* the case of 1 wt% water, hydrangea-like SnO balls with an average diameter of about 1–1.5 μm particles are formed, which are constructed by plenty of self-assembly SnO thin slices each with a thickness of about 5–10 nm.³⁹ When the reaction system containing 5 or 15 wt% water, the original SnO ball becomes an open structure, as shown in

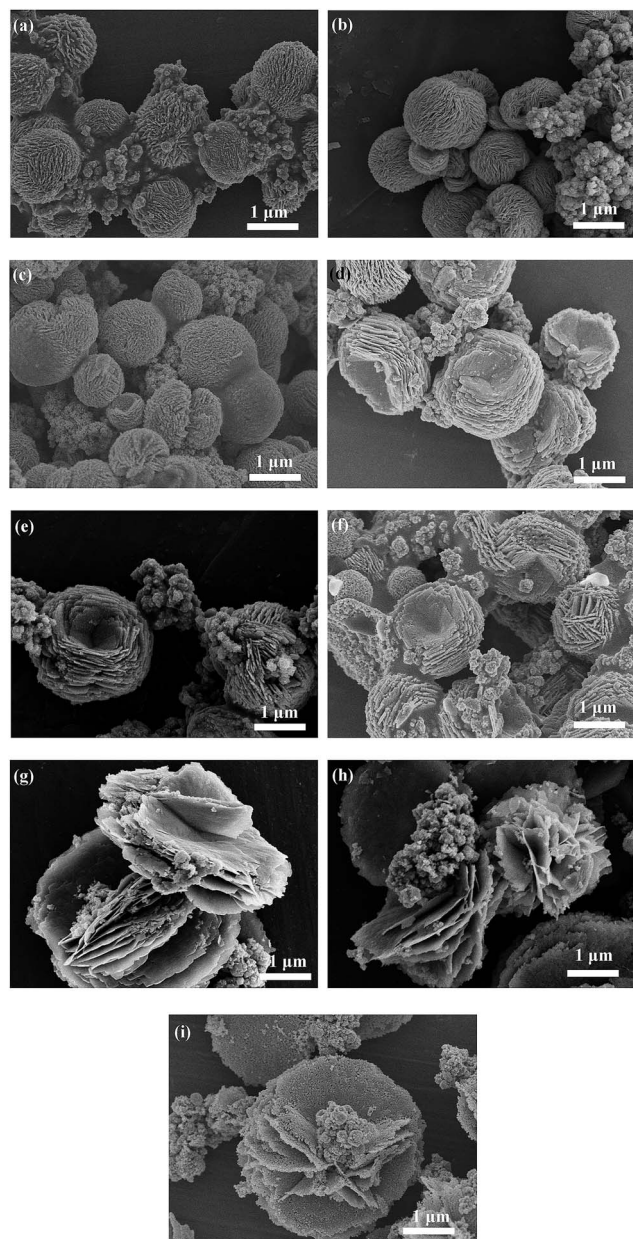


Fig. 2 SEM images of as-prepared SnO samples from different reaction systems with various water contents and their annealing products. (a) 1-SnO, (b) 1-400-SnO₂, (c) 1-600-SnO₂, (d) 5-SnO, (e) 5-400-SnO₂, (f) 5-600-SnO₂, (g) 15-SnO, (h) 15-400-SnO₂, (i) 15-600-SnO₂. TEM and HRTEM images and SAED of the prepared SnO samples.

Fig. 2d and g. The bowl-like SnO nanosheet with tens of nanometers of thickness is the layered building blocks for the SnO ensembles with open architectures. High density SnO nanosheets are assembled into 3D layered pancakes. The diameter of the multilayer pancake-like 15-SnO is about 3–4 μm , which is greater than that of the 5-SnO (1–2 μm) (see Fig. 2d and g). Moreover, the total number of layers in the multilayer pancake-like 5-SnO is greater than the one in 15-SnO. However, 15-SnO has a larger specific surface area than 5-SnO due to more space formed between SnO nanosheets. After the annealing process at 400 and 600 $^{\circ}\text{C}$, the geometry of the annealed product is retained as the as-prepared state. However, as for the 15-SnO sample, nanoporous structures significantly appear on the bowl-like SnO₂ nanosheet, as shown in Fig. 2i. The formation of pores should be resulting from the structure shrinking during the phase transformation from SnO to SnO₂.

The microstructure of the synthesized SnO and their annealed samples with different shapes were further characterized by TEM observations. The crystallography of these samples was investigated by using the selected area electron diffraction (SAED) and HRTEM imaging. The detailed TEM characterization of the 1-SnO sample can be found in our previous work.³⁹ The 1-SnO shows a quasi-mesocrystal structure consisting of tiny SnO and SnO₂ grains with size of about 4–6 nm. Fig. 3b and d give the TEM images of the 1-SnO after annealing process at 400 $^{\circ}\text{C}$ (*i.e.* 1-400-SnO₂) and 600 $^{\circ}\text{C}$ (*i.e.* 1-600-SnO₂) for 2 h, respectively. The SAED patterns of 1-400-SnO₂ shown in Fig. 3a are a mixture of the o-SnO₂ and t-SnO₂, which is attributed to the mixed phase structure of the sample. The SAED patterns are formed by discrete spots, which indicate that the crystal grains are ready to be aligned with a certain

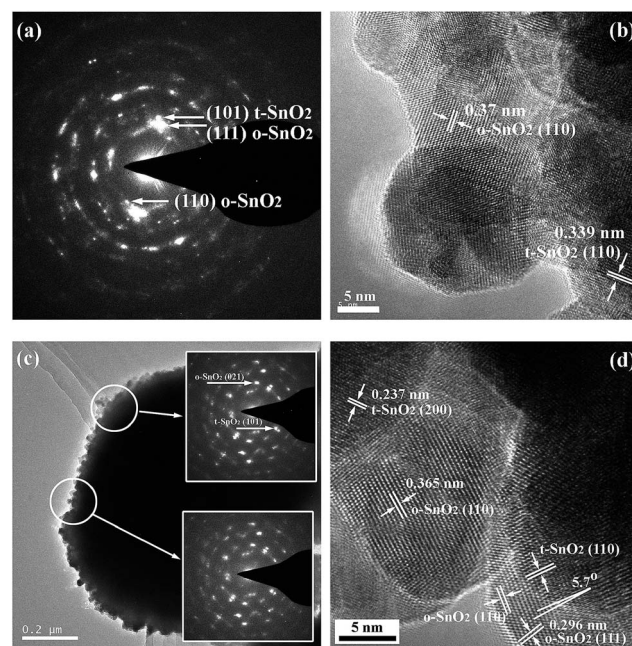


Fig. 3 TEM and HRTEM observations of 1-400-SnO₂ (b) and 1-600-SnO₂ samples (c and d). (a) is the SAED patterns for 1-400-SnO₂. The insets in (c) are SEAD patterns corresponding to the selected areas indicated by circles.

crystal orientation in 1-400-SnO₂. As indicated in Fig. 3a, the (101) planes of t-SnO₂ and the (110) planes of o-SnO₂ have close plane spacing, and they are parallel with each other. As shown in Fig. 3b, the 1-400-SnO₂ is composed of nanocrystalline o- and t-phase SnO₂ with an average grain size of about 10–30 nm. The plane fringes with 0.370 nm and 0.339 nm can be observed, which correspond to o-SnO₂ (110) and t-SnO₂ (110) crystalline plane spacings, respectively. The mixed phase of o- and t-SnO₂ is also observed when the 1-SnO is annealed at 600 °C, as revealed by SEAD patterns in Fig. 3c and HRTEM images of Fig. 3d. The very clear o-SnO₂ (110) plane fringes with 0.365 nm can be seen in Fig. 3d. As shown in the bottom-right of Fig. 3d, one t-phase grain and one o-phase grain are overlapped leaving an angle of about 5.7° between t-SnO₂ (110) and o-SnO₂ (111).

It is surprising to find that 5-SnO and 15-SnO nanosheet assembled pancakes show a single crystal nature, as shown in Fig. 4a and 5a. Typically, as shown in Fig. 5a, both SAED patterns corresponding to the edge and center regions of the SnO pancake look the same, showing the [00–2] zone diffraction. However, from the HRTEM images it can be seen the SnO samples are composed of numerous small nanoparticles roughly 2–5 nm in size (see Fig. 4b and 5b). Both the inset of Fig. 4b and 5b show a portion of a crystal formed by aggregation of SnO grains, which are characterized by sharing common

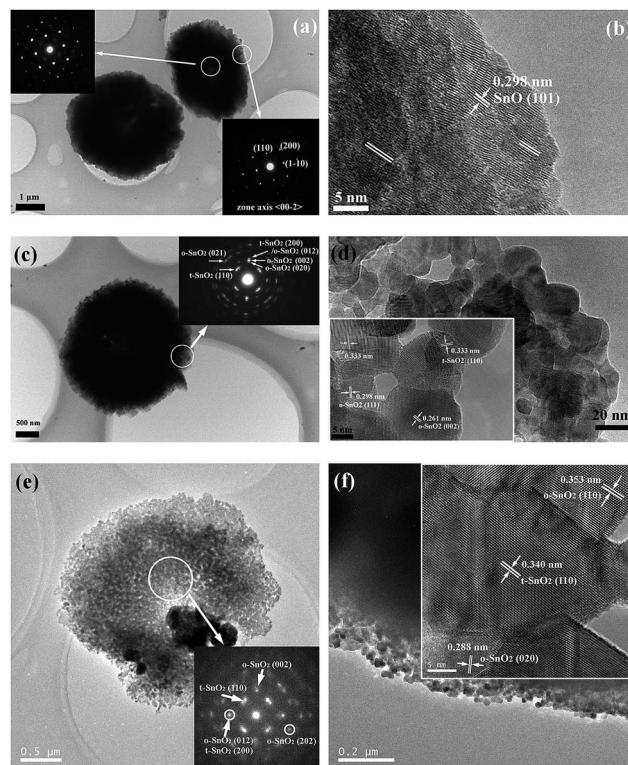


Fig. 5 TEM images and SEAD patterns of 15-SnO (a and b), 15-400-SnO₂ (c and d), and 15-600-SnO₂ samples (e and f). The insets in (d and f) are the corresponding HRTEM images, showing porous structures and mixed SnO₂ phases.

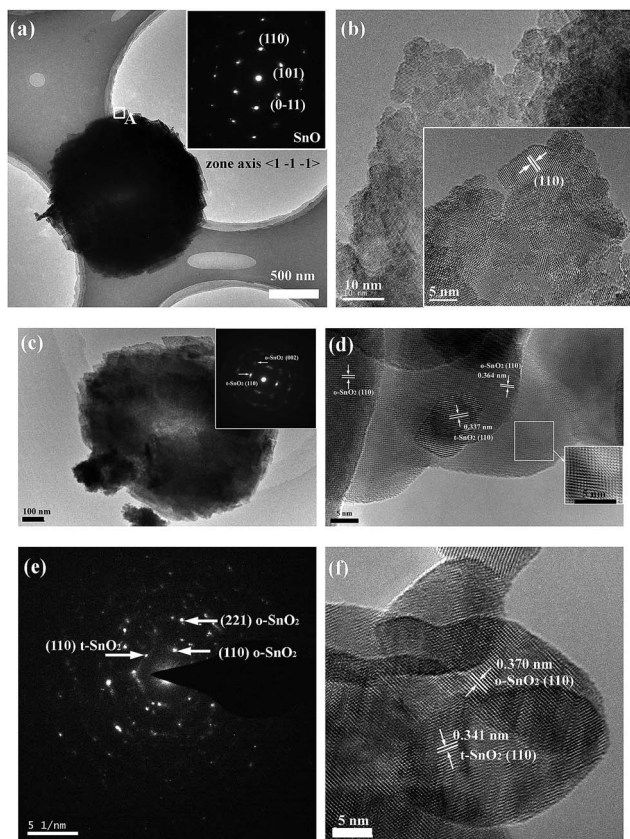


Fig. 4 TEM images and SEAD patterns of 5-SnO (a and b), 5-400-SnO₂ (c and d), and 5-600-SnO₂ samples (e and f). The inset in (d) is the Fourier-filtered lattice image for the selected area, showing clearly the existence of the orthorhombic phase of SnO₂.

crystallographic orientations. Oriented attachment involves the spontaneous self-organization of adjacent particles so that they share a common crystallographic orientation, followed by joining these particles at a planar interface, thus leading to the formation of a new single crystal.^{40,41} After this step, an oriented attachment process occurring by means of grain rotation may decrease the angle of misorientation, changing the orientation of the grains.^{50,51} Inorganic mesocrystals *via* a SA process of nanoparticles are of both theoretical and technological interest due to their size/shape-dependent applications and properties on a nanometer scale.^{52,53} In contrast to the classical mechanism of atom/molecule based growth of a single crystal, the particle mediated growth and SA mechanisms are termed as “non-classical crystallization”, including oriented attachment and mesocrystal formation.^{42,43} In this case, the SnO mesocrystals should be formed by the non-classical crystallization mechanism, which is driven by the elimination of pairs of high energy surfaces between particles from the thermodynamic viewpoint. With the annealing process, the grain size of the 5-400-SnO₂ or the 5-600-SnO₂ is significantly increased to about 50–70 nm, as shown in Fig. 4d and f. Moreover, the mixed phase nature of t- and o-SnO₂ is clearly distinguished. One rectangle-shaped t-SnO₂ grain embedded in an o-SnO₂ grain is observed in Fig. 4d. The lattice fringes with lattice spacings of 0.337 and 0.364 nm are in good agreement with the *d* values of the (110) and (110) lattice spacings of t-SnO₂ and o-SnO₂ crystals.

Interestingly, the nanoporous structure is formed in 15-400-SnO₂ and 15-600-SnO₂, as shown in Fig. 5c–f. The pore size is in the range of 4–10 nm, and the pore ligament is constructed by mixed phase of SnO₂. The SAED patterns shown in Fig. 4c, d and 5c, d also indicate the mesocrystal nature of the mixed phase SnO₂. The grain size of 15-600-SnO₂ is about 50 nm, which is larger than that of 15-400-SnO₂ (~20 nm). Fig. 6a gives the N₂ adsorption (open symbols) and desorption (solid symbols) isotherms at 200 °C of the SnO₂ samples, which were obtained by annealing the SnO samples at 400 °C, from which it can be seen that the 15-400-SnO₂ sample has the largest specific surface area of 23.928 m² g^{−1}. Clearly, the obvious porous structure endows the 15-γ-SnO₂ with a higher specific surface area than does the 1-γ-SnO₂ and 5-γ-SnO₂ samples. The BJH pore size distribution of the 400 °C annealed samples is shown in Fig. 6b, which indicates the 15-400-SnO₂ sample exhibits a bimodal pore size distribution. There are pores with an average size of about 10 nm in all 400 °C annealed samples, which is consistent with the TEM observations. However, besides the 10 nm sized pores, the pores with a size of about 25 nm are also significant in the 15-400-SnO₂ sample.

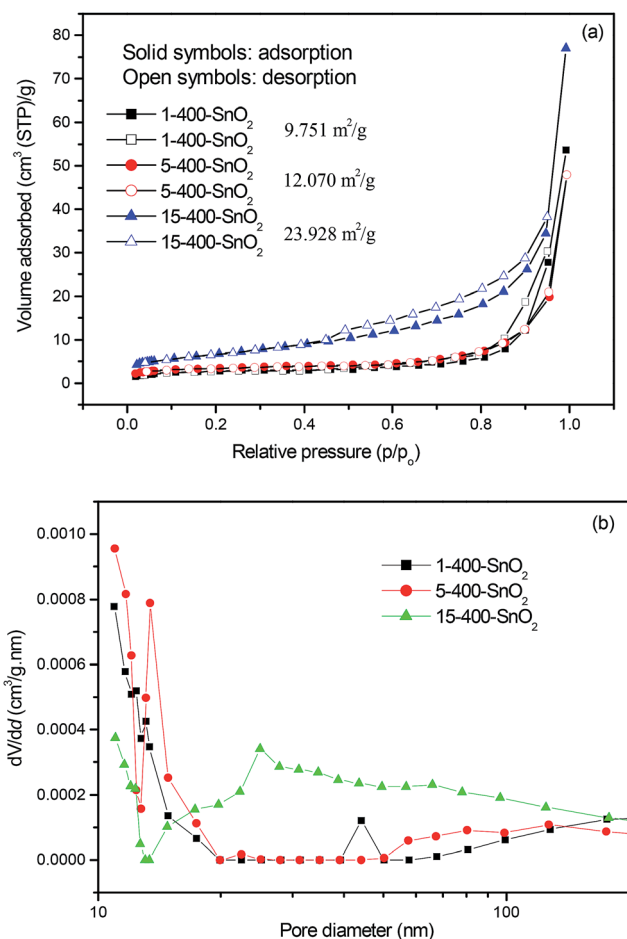
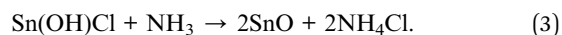


Fig. 6 (a) N₂ adsorption (open symbols) and desorption (solid symbols) isotherms at 200 °C of the SnO₂ samples. (b) BJH pore size distribution derived from the adsorption branch of the isotherm as shown in (a).

Based on the microstructure characterizations shown above, we proposed a mechanism to discuss the formation of mixed phase of SnO₂ mesocrystals, which is illustrated in Fig. 7. The structures of SnO are determined by a “mesocrystal formation” process in the CU mixture using water as the morphology controlling agent. Without the addition of surfactants, only CU solvent and SnCl₂ are needed in the reaction system, in which the CU acts as reaction medium as well as control agent for particle growth. The chemical reaction for the ionothermal synthesis of SnO is described as follows:



In the synthetic process, the CO(NH₂)₂ portion in the CU breaks up to release NH₃ at around 100 °C.⁵⁴ The slow-releasing NH₃ reacts with Sn(OH)Cl, which is a Sn²⁺ hydrolysis product to form the SnO nucleus. The SnO nucleation clusters grow or integrate together into the larger primary nanoparticles with a size of about 5 nm, which are the building blocks for the following SA process of SnO particles *via* a non-classical crystallization mode. Non-classical crystallization events are always particle mediated and involve a mesoscopic transformation process.⁵⁵ The geometry change of SnO ensemble from quasi-mesocrystal ball to perfect-mesocrystal pancake should be attributed to the water content in the reaction system. We propose three reasons to illustrate the SnO mesocrystal formation. First, water has a lower viscosity and density than does CU-based DES, resulting in a decrease of the values of both properties upon increasing the water content.⁵⁶ When increasing the water content in the CU solution, the viscosity of the solution decreases. Lower viscosity benefits the SA process of SnO nucleation clusters in the view of orientation mechanism.

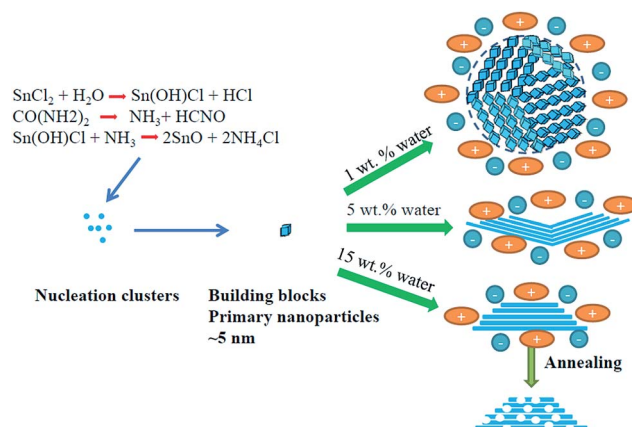


Fig. 7 Schematic map of the self-assembly process of the SnO_x mesocrystals and the topotactic transformation under the annealing process. The number of cations and anions around the SnO particles represent the polarity of the medium. The ions play a structure-directing role in the SA process.

Therefore, 15-SnO and 5-SnO have a perfect mesocrystal structure compared with 1-SnO. Second, more water promotes the hydrolysis process of Sn^{2+} as shown in eqn (1), thus leading to high reaction kinetics. Therefore, the water adding system produces smaller grain sized SnO. Moreover, during the synthesis process it is found that the amount of product from the water-adding system is larger than that from the lower water content system due to more SnO nucleation clusters formed. Last but more importantly, the polarity of the medium is suggested to play a structure-directing role for the particle mediated crystallization process.⁴⁸ Recently, we demonstrated the self-assembly of MnCO_3 particles into well-defined rhombohedral mesocrystals, ellipsoidal polycrystal ensembles, and nanoparticulate aggregates without addition of any surfactant *via* a non-classical crystallization route in the CU-based system.⁴⁸ The underlying mechanism of the shape transformation of MnCO_3 particles is discussed based on the decrease of polarity and the decomposition event of the CU medium upon heat treatments.⁴⁸ It is rational that the polarity of the medium gradually decreases along with the precipitation of SnO particles. Plenty of ions including cations and anions exist in the CU system, which will screen the dipoles inside the crystals, thus helping the arrangement of the primary SnO nanoparticles into SnO ensembles *via* oriented attachment. The polarity decrease is significant in the more water system, which leads to the multilayered pancake-like SnO ensembles with open structures under the less ions shielding condition, as indicated in Fig. 7. The formation of a quasi-mesocrystal SnO solid ball (*i.e.* 1-SnO) should be attributed to a viscous drag force from the surrounding liquids during the SA process of nanoparticles.

The mesocrystal SnO_2 is formed by a simple topotactic transformation during the annealing process. As indicated above, the o-phase of SnO_2 is an intermediate phase during the transformation of tetragonal SnO to tetragonal SnO_2 , which is the high temperature stable phase. The mesocrystal SnO holds a relatively higher thermal stability⁵² and the mixed phase of SnO_2 can be found when heating the SnO at 400 and 600 °C. However, the higher temperature of 900 °C makes the phase change of SnO sufficient to be a stable t-phase SnO_2 .

The mixed phase SnO_2 mesocrystals resulting from directly annealing SnO is further evaluated to detect ethanol as typical gas sensor application. Because the sensing characteristic of semiconductor oxide to a specific gas is largely dependent on the working temperature, it is necessary to find out the optimum operating temperature for our samples. Fig. 8 shows the response plots of these sensors to 200 ppm ethanol at operating temperatures from 160–400 °C. It can be seen that the response of the SnO_2 samples obtained at 400 and 600 °C annealing processes increases with increasing temperature and reaches to a peak at ~300 °C, then decreases when there is further increase in the operating temperature. Significantly, the response of mixed phase SnO_2 (*i.e.* the annealing samples at 400 and 600 °C) is always higher than that of the single t-phase SnO_2 obtained by annealing SnO at 900 °C, which should be attributed to the existence of the o- SnO_2 in the SnO_2 mesocrystals. As shown in Fig. 8d, among all the 400 °C annealed

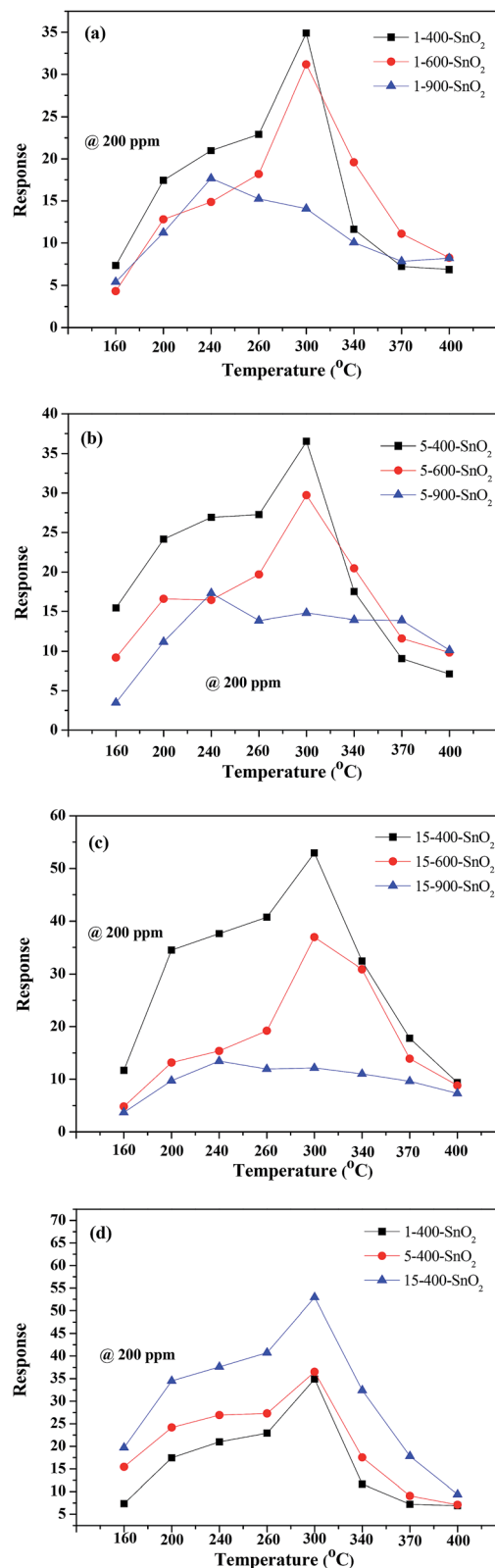
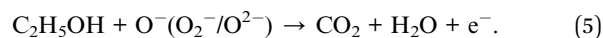
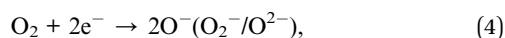


Fig. 8 Gas response of the SnO_2 mesocrystals to 200 ppm ethanol as a function of operating temperature. (a) SnO_2 samples annealed from 1-SnO; (b) SnO_2 samples annealed from 5-SnO; (c) SnO_2 samples annealed from 15-SnO; (d) SnO_2 samples from annealing corresponding SnO precursors at 400 °C.

samples, the 15-400-SnO₂ exhibits the highest sensor response when exposed to 200 ppm ethanol. At the optimum operating temperature of 300 °C, the response of 15-400-SnO₂ reaches to about 52.9, which is ~1.5 times higher than those of the other two samples of 1-400-SnO₂ and 5-400-SnO₂.

Fig. 9 gives the gas response of the studied SnO₂ mesocrystals based sensors to various ethanol concentrations (5–1000 ppm) at the optimum operating temperature of 300 °C. It can be clearly seen that the response increases quickly with increasing the ethanol concentration, and even at the lowest concentration 5 ppm of ethanol, the response values are still larger than 3, which is a practicable value to detect lower concentration ethanol. Moreover, we can also observe that the samples annealed at 400 °C of all the three groups show the largest response values than do the other two samples in each group. This result can be attributed to the different phase contents in the different samples. From the XRD analysis, the sample annealed at 400 °C contains the most amount of o-SnO₂, which reaches about 40.4 wt% and 38.7 wt% for the 1-400-SnO₂ and 15-400-SnO₂, respectively. As for the 15-600-SnO₂, the o-SnO₂ only consists 29.0 wt% of the entire sample. From this point of view, we can see that the o-SnO₂ fraction in the mixed phased plays an important role in enhancing the sensitivity of the SnO₂ towards ethanol gas. The larger the fraction of the o-SnO₂ phase, the higher the response of the SnO₂. On the other hand, we can see from Fig. 8d the response of the three samples is ranked as 15-400-SnO₂ > 5-400-SnO₂ > 1-400-SnO₂. As shown in Fig. 6, the 15-400-SnO₂ sample has the largest BET surface area and a bimodal pore size distribution, which should be responsible for its higher response sensitivity among the 400 °C annealed samples.

The gas sensing mechanism of the ethanol detection using SnO₂ composites can be illustrated to follow the adsorption–oxidation–desorption pathway. For the SnO₂-based sensing material, the space-charge layer mode⁵⁷ can be used to explain the high sensing performance. When the sensing material is exposed to oxygen (O₂) in air or ambient, the surface of the sensing material adsorbs oxygen, which will extract electrons in the bulk and be ionized. Then, at the surface of the material chemisorbed oxygen species (O₂[−], O[−], O^{2−}) will be created, which cause a narrow conduction channel. Consequently, depletion layers will be formed in the surface area of SnO₂, which cause the decrease of the carrier concentration and leads to a high resistance of the sensor.⁵⁸ When exposed to reducing gas ethanol, the ethanol molecules will react with the absorbed ions (O₂[−], O[−], O^{2−}) and the conduction channel becomes wider. The trapped electrons are released back to the conduction band, and then the carrier concentration of SnO₂ will increase.⁵⁸ It can be proposed that there were the following reactions near the interface:⁵⁹



As it is reported that the o-SnO₂ has a wider band gap ($E_g = 4.02$ eV) than that of the t-SnO₂ ($E_g = 3.73$ eV).²⁸ It means

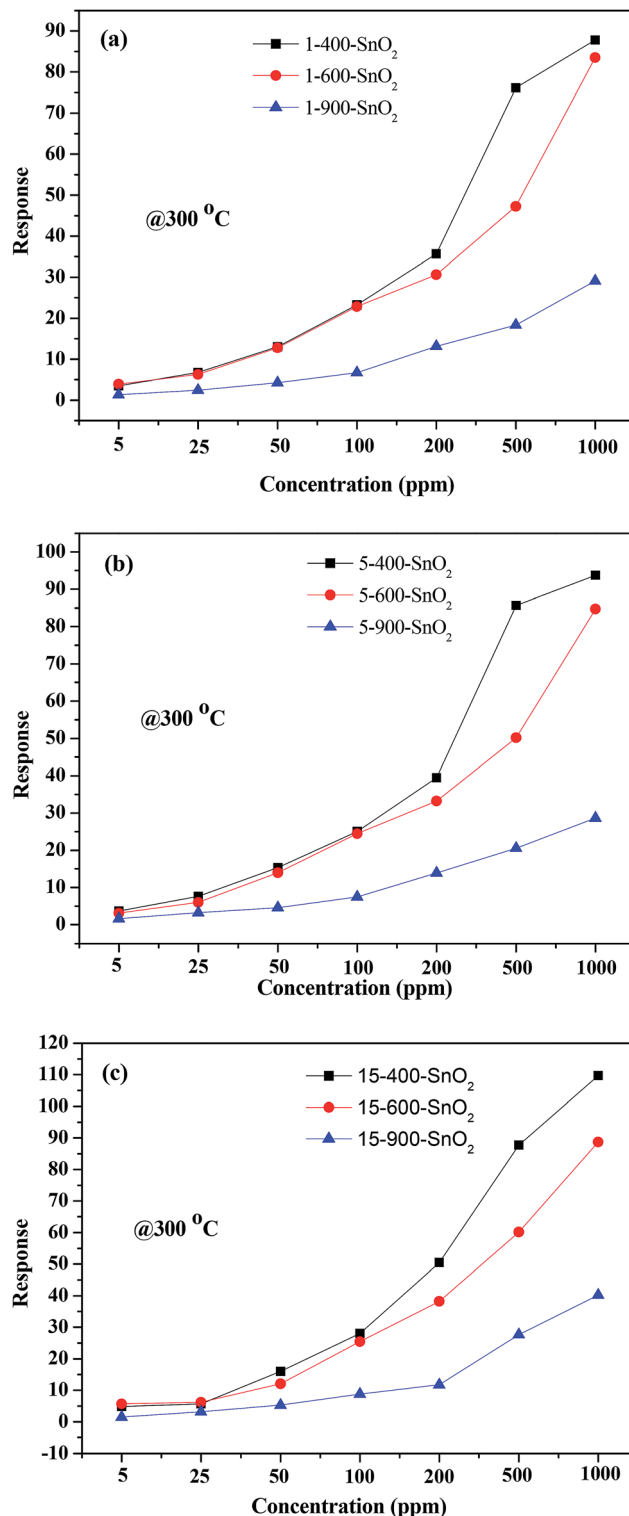


Fig. 9 Gas response of the SnO₂ mesocrystal based sensors to various ethanol concentrations (5–1000 ppm) at the optimum operating temperature of 300 °C. (a) SnO₂ samples annealed from 1-SnO; (b) SnO₂ samples annealed from 5-SnO; (c) SnO₂ samples annealed from 15-SnO.

that the mixed tin dioxide phase has a larger resistance than pure SnO₂. When exposed to the ethanol gas, the reduced resistance may be more pronounced than in pure SnO₂, which

Table 1 The gas sensing performance of ethanol based on the present SnO₂ mesocrystal (*i.e.* 15-400-SnO₂) and the SnO₂ nanostructures reported in the literature^{23,60–62}

| Materials | Ethanol (ppm) | Operating temperature (°C) | Sensitivity | References |
|--------------------------------|---------------|----------------------------|-------------|-------------------------|
| This work | 100 | 300 | 28.06 | 15-400-SnO ₂ |
| SnO ₂ nanowire | 100 | 400 | 11.5 | 60 |
| SnO ₂ nanorods | 100 | 300 | 13.9 | 61 |
| SnO ₂ nanofibers | 100 | 300 | <20 | 23 |
| SnO ₂ nanoparticles | 100 | 220 | 24.35 | 62 |

contributed to the larger response of the SnO₂ with mixed phase. Significantly, our mixed phase SnO₂ mesocrystal has a distinguished gas sensor sensitivity over the other reported nanostructured SnO₂, including the forms of nanowire, nanorods, nanofibers, and nanoparticle, which are summarized in Table 1.

The response transient to 200 ppm ethanol gas of the SnO₂ mesocrystal gas sensors measured at 300 °C is shown in Fig. 10, which is used to measure the response/recovery time of the 1-400-SnO₂, 5-400-SnO₂, and 15-400-SnO₂. The corresponding response/recovery time values are listed in Table 2. As shown in Table 2, the response times of the three samples are all 2 s, which demonstrate that the mixed phase SnO₂ mesocrystal based sensors have rapid responses. For the recovery time, it follows the order 1-400-SnO₂ (29 s) > 5-400-SnO₂ (86 s) > 15-400-SnO₂ (130 s), which can be ascribed to the different specific surface areas of the three samples. We know that ethanol gas molecules are in dynamic equilibrium of adsorption and desorption on the surface of the SnO₂. A longer recovery time of the 15-400-SnO₂ should be related to its porous nanostructure and larger specific surface area.

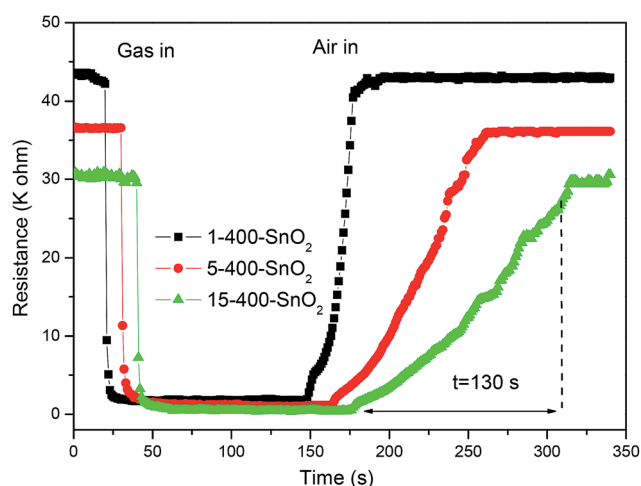
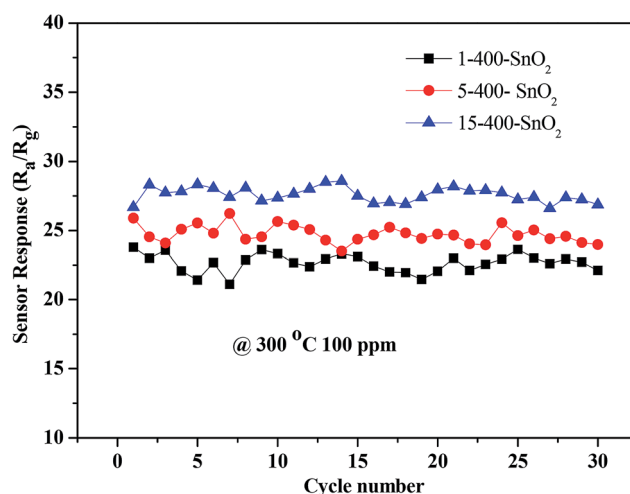
It is well known that the sensor reliability is strongly dependent on the reproducibility and stability exhibited by the sensor material. Fig. 11 shows the reproducibility of the SnO₂ mesocrystal gas sensors standing for 100 ppm ethanol at the optimum operating temperature of 300 °C by repeating the

Table 2 The response and recovery time of the SnO₂ mesocrystal gas sensors under standing conditions for 200 ppm ethanol gas and at the optimum operating temperature of 300 °C, which was revealed from Fig. 10

| 200 ppm ethanol gas @ 300 °C | Response time (s) | Recovery time (s) |
|------------------------------|-------------------|-------------------|
| 1-400-SnO ₂ | 2 | 29 |
| 5-400-SnO ₂ | 2 | 86 |
| 15-400-SnO ₂ | 2 | 130 |

response measurement 30 times. Clearly, it can be seen that the response of all the three SnO₂-based sensors keeps almost constant during 30 response times, which can fully demonstrate the stability of the mixed phase SnO₂ mesocrystals. Furthermore, the response of the three samples follows the order: 15-400-SnO₂ > 5-400-SnO₂ > 1-400-SnO₂, which is consistent with the results as shown in Fig. 8d.

The cross-selectivity of the sensor based on the 15-400-SnO₂ mesocrystal gas sensor was investigated by measuring the response of sensor against some typical gases, including acetone, methanol, and benzene (experiments were carried out at various temperatures with gaseous concentration of 200 ppm). It is obvious that the 15-400-SnO₂ mesocrystal gas

**Fig. 10** Response transient to 200 ppm ethanol gas of the SnO₂ mesocrystal gas sensors measured at 300 °C.**Fig. 11** Cyclic gas response of the SnO₂ mesocrystal gas sensors towards 100 ppm ethanol at the optimum operating temperature of 300 °C.

sensor showed high selectivity towards ethanol among all the gases as shown in Fig. 12, especially at the optimum operation temperature of 300 °C. During the environmental ethanol monitoring, good discrimination of ethanol from acetone is very important for ethanol sensors in practice because of which the cross-sensitivity between ethanol and acetone is very similar.⁶ Fig. 12b shows the discrimination of ethanol from acetone based on 15-400-SnO₂ mesocrystals at various operation temperatures. As shown in Fig. 12b, it can be clearly observed that mixed phase SnO₂ mesocrystals showed high selectivity towards ethanol. The response to ethanol and acetone gradually increased with the operation temperature and reaches a maximum value at the optimum operating temperature of 300 °C. Above 300 °C, the response to ethanol is significantly decreased. At 200 °C, the response to ethanol is about 34.5. However, the response to acetone is only about 1.2. The ratio of response to ethanol over acetone ($R_{\text{ethanol}}/R_{\text{acetone}}$) is as high as 28.7 at the operation temperature of 200 °C. The value of $R_{\text{ethanol}}/R_{\text{acetone}}$ is still high to 6.6 at the operation

temperature of 260 °C, which indicates that good discrimination of ethanol from acetone has been realized in the mixed phase SnO₂ mesocrystals.

4. Conclusion

In summary, we developed a novel ionothermal strategy using the ChCl/urea-based DES to synthesize the SnO mesocrystals by facilely controlling the water content in the reaction system. The formation of the SnO mesocrystals is related to a “non-classical crystallization” process involving an oriented attachment mechanism. Significantly, directly annealing the SnO particles at ambient-pressure to produce the metastable o-SnO₂ has been realized. The SnO₂ mesocrystals with mixed phases (*i.e.*, tetragonal and orthorhombic phase) and nanoporous structures were obtained *via* a topotactic transformation of SnO precursors under ambient-pressure and a moderate annealing temperature range of 400–600 °C. The mixed phase and nanoporous SnO₂ mesocrystal exhibits superior ethanol sensitivity compared with the SnO₂ with a single phase or a solid structure, which is due to incorporating orthorhombic and tetragonal phases and the porous structure. Additionally, good discrimination of ethanol from acetone has been realized in the mixed phase SnO₂ mesocrystals.

Acknowledgements

This work was supported by the National Natural Science Foundation of China (51271169), the Key Science and Technology Innovation Team of Zhejiang Province under grant number 2010R50013, and the Program for Innovative Research Team in University of Ministry of Education of China (IRT13037).

References

- 1 S. Das and V. Jayaraman, *Prog. Mater. Sci.*, 2014, **66**, 112.
- 2 G. Korotcenkov, *Mater. Sci. Eng., B*, 2007, **139**, 1.
- 3 J. Huang, N. Matsunaga, K. Shimanoe, N. Yamazoe and T. Kunitake, *Chem. Mater.*, 2005, **17**, 3513.
- 4 H. C. Chiu and C. S. Yeh, *J. Phys. Chem. C*, 2007, **111**, 7256.
- 5 G. Zhang and M. L. Liu, *Sens. Actuators, B*, 2000, **69**, 144.
- 6 Z. Jiang, T. Jiang, J. Wang, Z. Wang, X. Xu, Z. Wang, R. Zhao, Z. Li and C. Wang, *J. Colloid Interface Sci.*, 2015, **437**, 252.
- 7 C. X. Wang, D. P. Cai, B. Liu, H. Li, D. D. Wang, Y. Liu, L. L. Wang, Y. R. Wang, Q. H. Li and T. H. Wang, *J. Mater. Chem. A*, 2014, **2**, 10623.
- 8 W. Zhang, J. L. Tian, Y. A. Wang, X. T. Fang, Y. Q. Huang, W. X. Chen, Q. L. Liu and D. Zhang, *J. Mater. Chem. A*, 2014, **2**, 4543.
- 9 F. Li, Y. J. Chen and J. M. Ma, *J. Mater. Chem. A*, 2014, **2**, 7175.
- 10 Z. Y. Li, X. G. Wang and T. Lin, *J. Mater. Chem. A*, 2014, **2**, 13655.
- 11 N. Yamazoe, *Sens. Actuators, B*, 2005, **108**, 2.
- 12 M. Nakagawa and N. Yamashita, in *Frontiers in Chemical Sensors*, ed. G. Orellana and M. Moreno-Bondi, Springer, Berlin Heidelberg, 2005, vol. 3, p. 93.

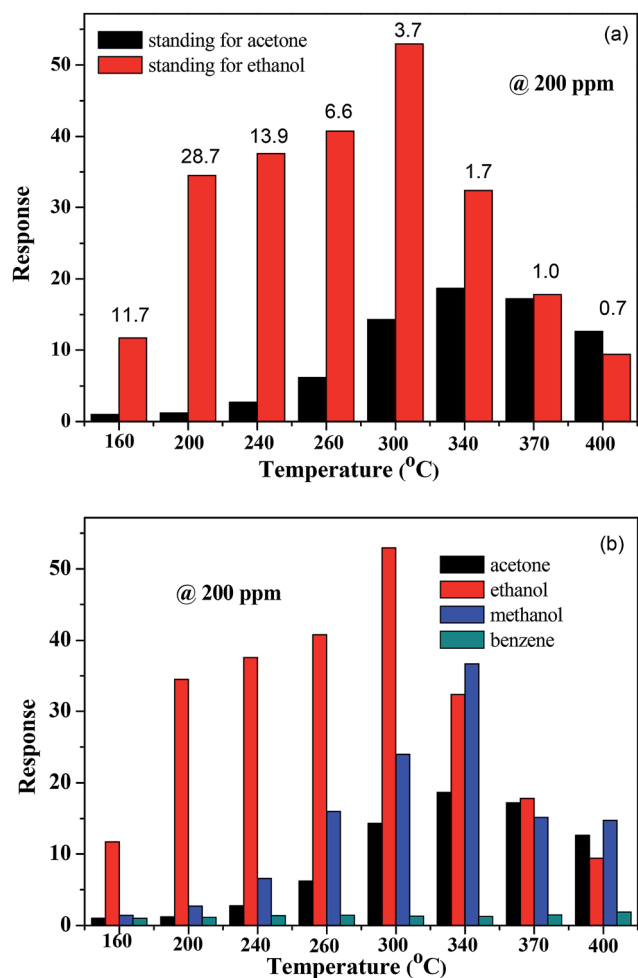


Fig. 12 (a) Cross-sensitivities of the 15-400-SnO₂ mesocrystal gas sensor to ethanol, acetone, methanol, and benzene. (b) Discrimination of ethanol from acetone of the 15-400-SnO₂ mesocrystal gas sensor under various operation temperatures. The numbers shown in the figure is the ratio of response to ethanol over acetone ($R_{\text{ethanol}}/R_{\text{acetone}}$).

- 13 N. Na, S. Zhang, S. Wang and X. Zhang, *J. Am. Chem. Soc.*, 2006, **128**, 14420.
- 14 S. Li, J. Zheng, W. Zhang, J. Cao, S. Li and Z. Rao, *Analyst*, 2013, **138**, 916.
- 15 L. Yu, L. Zhang, H. Song, X. Jiang and Y. Lv, *CrystEngComm*, 2014, **16**, 3331.
- 16 J. Zheng, W. Zhang, J. Cao, X. Su, S. Li, S. Hu, S. Li and Z. Rao, *RSC Adv.*, 2014, **4**, 21644.
- 17 J. Zheng, Z. Xue, S. Li, S. Li and Z. Rao, *Anal. Methods*, 2012, **4**, 2791.
- 18 Z. Li, Q. Zhao, W. Fan and J. Zhan, *Nanoscale*, 2011, **3**, 1646.
- 19 A. Kar and A. Patra, *J. Mater. Chem. C*, 2014, **2**, 6706.
- 20 G. J. Li, X. H. Zhang and S. Kawi, *Sens. Actuators, B*, 1999, **60**, 64.
- 21 Y. Nakamura, H. Yoshioka, M. Miyayama, H. Yanagida, T. Tsurutani and Y. Nakamura, *J. Electrochem. Soc.*, 1990, **137**, 940.
- 22 H. Wang, L. Xi, J. Tucek, Y. Zhan, T. F. Hung, S. V. Kershaw, R. Zboril, C. Y. Chung and A. L. Rogach, *Nanoscale*, 2013, **5**, 9101.
- 23 Y. Zhang, X. He, J. Li, Z. Miao and F. Huang, *Sens. Actuators, B*, 2008, **132**, 67.
- 24 J. Haines and J. M. Léger, *Phys. Rev. B: Condens. Matter Mater. Phys.*, 1997, **55**, 11144.
- 25 L. Sangaletti, L. E. Depero, A. Dieguez, G. Marca, J. R. Morante, A. Romano-Rodriguez and G. Sberveglieri, *Sens. Actuators, B*, 1997, **44**, 268.
- 26 J.-P. Ahn, S.-H. Kim, J.-K. Park and M.-Y. Huh, *Sens. Actuators, B*, 2003, **94**, 125.
- 27 D. Hu, B. Han, S. Deng, Z. Feng, Y. Wang, J. Popovic, M. Nuskol, Y. Wang and I. Djerdj, *J. Phys. Chem. C*, 2014, **118**, 9832.
- 28 Z. W. Chen, C. M. L. Wu, C. H. Shek, J. K. L. Lai, Z. Jiao and M. H. Wu, *Crit. Rev. Solid State Mater. Sci.*, 2008, **33**, 197.
- 29 K. Suito, N. Kawai and Y. Masuda, *Mater. Res. Bull.*, 1975, **10**, 677.
- 30 F. J. Lamelas, *J. Appl. Phys.*, 2004, **96**, 6195.
- 31 H. Deng, F. J. Lamelas and J. M. Hossenlopp, *Chem. Mater.*, 2003, **15**, 2429.
- 32 F. J. Lamelas and S. A. Reid, *Phys. Rev. B: Condens. Matter Mater. Phys.*, 1999, **60**, 9347.
- 33 H. Fan and S. A. Reid, *Chem. Mater.*, 2003, **15**, 564.
- 34 V. Kraševac, A. Prodan, M. Hudomalj and S. Sulčić, *Phys. Status Solidi A*, 1985, **87**, 127.
- 35 A. Prodan, N. Vene, F. Sevšek and M. Hudomalj, *Thin Solid Films*, 1987, **147**, 313.
- 36 B. Lu, C. S. Wang and Y. H. Zhang, *Appl. Phys. Lett.*, 1997, **70**, 717.
- 37 L. Sangaletti, L. E. Depero, A. Dieguez, G. Marca, J. R. Morante, A. Romano-Rodriguez and G. Sberveglieri, *Sens. Actuators, B*, 1997, **44**, 268.
- 38 J. Arbiol, E. Comini, G. Faglia, G. Sberveglieri and J. R. Morante, *J. Cryst. Growth*, 2008, **310**, 253.
- 39 H. Zheng, C. D. Gu, X. L. Wang and J. P. Tu, *J. Nanopart. Res.*, 2014, **16**, 2228.
- 40 E. L. Smith, A. P. Abbott and K. S. Ryder, *Chem. Rev.*, 2014, **114**, 11060.
- 41 D. V. Wagle, H. Zhao and G. A. Baker, *Acc. Chem. Res.*, 2014, **47**, 2299.
- 42 A. P. Abbott, D. Boothby, G. Capper, D. L. Davies and R. K. Rasheed, *J. Am. Chem. Soc.*, 2004, **126**, 9142.
- 43 C. D. Gu, Y. J. Mai, J. P. Zhou, Y. H. You and J. P. Tu, *J. Power Sources*, 2012, **214**, 200.
- 44 C. D. Gu and J. P. Tu, *Langmuir*, 2011, **27**, 10132.
- 45 C.-D. Gu and J.-P. Tu, *RSC Adv.*, 2011, **1**, 1220.
- 46 X. Ge, C. D. Gu, Y. Lu, X. L. Wang and J. P. Tu, *J. Mater. Chem. A*, 2013, **1**, 13454.
- 47 X. Ge, C. D. Gu, X. L. Wang and J. P. Tu, *J. Mater. Chem. A*, 2014, **2**, 17066.
- 48 X. Ge, C. D. Gu, X. L. Wang and J. P. Tu, *J. Colloid Interface Sci.*, 2015, **438**, 149.
- 49 C. H. Shek, J. K. L. Lai, G. M. Lin, Y. F. Zheng and W. H. Liu, *J. Phys. Chem. Solids*, 1997, **58**, 13.
- 50 J. X. Fang, X. N. Ma, H. H. Cai, X. P. Song and B. J. Ding, *Nanotechnology*, 2006, **17**, 5841.
- 51 C. D. Gu and T. Y. Zhang, *Langmuir*, 2008, **24**, 12010.
- 52 T. Tachikawa and T. Majima, *NPG Asia Mater.*, 2014, **6**, e100.
- 53 A. J. Blake, N. R. Champness, P. Hubberstey, W.-S. Li, M. A. Withersby and M. Schröder, *Coord. Chem. Rev.*, 1999, **183**, 117.
- 54 C. Gu, H. Zhang, X. Wang and J. Tu, *RSC Adv.*, 2013, **3**, 11807.
- 55 M. Niederberger and H. Colfen, *Phys. Chem. Chem. Phys.*, 2006, **8**, 3271.
- 56 M. Francisco, A. van den Bruinhorst and M. C. Kroon, *Angew. Chem., Int. Ed.*, 2013, **52**, 3074.
- 57 I. Hafaiedh, S. Helali, K. Cherif, A. Abdelghani and G. Tournier, *Mater. Sci. Eng., C*, 2008, **28**, 584.
- 58 Z. Wang, Z. Li, J. Sun, H. Zhang, W. Wang, W. Zheng and C. Wang, *J. Phys. Chem. C*, 2010, **114**, 6100.
- 59 Y. Chen, L. Yu, D. Feng, M. Zhuo, M. Zhang, E. Zhang, Z. Xu, Q. Li and T. Wang, *Sens. Actuators, B*, 2012, **166–167**, 61.
- 60 N. Van Hieu, H.-R. Kim, B.-K. Ju and J.-H. Lee, *Sens. Actuators, B*, 2008, **133**, 228.
- 61 Y. J. Chen, X. Y. Xue, Y. G. Wang and T. H. Wang, *Appl. Phys. Lett.*, 2005, **87**, 233503.
- 62 J. Zhang, S. Wang, Y. Wang, M. Xu, H. Xia, S. Zhang, W. Huang, X. Guo and S. Wu, *Sens. Actuators, B*, 2009, **139**, 369.